physica status solidi b
www.pss-b.com

First-Principles Calculations to Investigate the Structural, Mechanical, Electronic, Optical and Thermal Properties of Disilicides Materials UT_2Si_2 (T = Ru, Rh, and Pd)

Md. Atikur Rahman, Mst. Asma Khatun, Md. Hasan Mia, Mst. Zugrufa, and Ahmad Irfan*

Different physical features of UT_2Si_2 (T = Ru, Rh, Pd) are investigated using *ab initio* methods. The examined lattice parameters are closely aligned with the experimental data. The negative cohesive energy ensures the chemical stability of the UT_2Si_2 (T = Ru, Rh, Pd). The mechanical stability of UT_2Si_2 (T = Ru, Rh, Pd) is ensured from the positive elastic constants. Very large bulk and Young's moduli of URu_2Si_2, and URh_2Si_2 ensures their high resistance to volume and longitudinal deformation. Whereas the lower Young's modulus (*E*) for UPd_2Si_2 suggests its heightened capacity to resist thermal shock resistance. The high machinable index of UPd_2Si_2 compared to URu_2Si_2 and URh_2Si_2 confirm its more damage-tolerant and high elastic behavior and probable industrial applications. All the phases exhibit elastic anisotropy and ductile nature. Metallic features as well as mixture of covalent and ionic bonding are observed from electronic properties. Furthermore, the investigation on optical properties suggests the potential use of UT_2Si_2 (T = Ru, Rh, Pd) in anti-reflection coatings, UV detectors, and optoelectronic devices due to their notable peaks in the UV energy range. The thermodynamic parameters such as Debye temperature as well as minimum thermal conductivity indicate the potential utility of these compounds in thermal barrier coating materials.

1. Introduction

Rare earth intermetallic compounds have been the subject of scientific exploration for half a century, driven by their diverse physical properties and potential technological applications. With forward-looking studies anticipating a significant increase in worldwide demand for energy in the next decades, driven mostly by population growth and the development of emerging economies, the need to address climate change requires the inclusion of nuclear energy into the global energy mix. The recent shift toward nuclear power utilization, observed in different countries, highlights its potential as a low-carbon-emission energy source to counteract the harmful effects of climate change.[1] Presently, nuclear power contributes significantly to electricity generation, accounting for 19.4% in the United States and 14% globally, with uranium playing a central role despite its infamous history associated with atomic bombings during World War II.[1,2]

While the focus on nuclear energy expands, scientific interest in rare earth intermetallic compounds remains effective, particularly in the family of AT_2X_2 composites (here, A is lanthanide or alkaline earth element, T denotes transition metal, X = P, Ge, Si, or As). These compounds, characterized by unusual physical properties such as heavy Fermion behavior, valence fluctuation, mixed valency, and superconductivity at both high and low temperatures, have gained interest from researchers. In 1965, Sikirica et al.[3] were first reported and described the crystal structure of $ThCr_2Si_2$-type compounds. Furthermore, the initial theoretical simulation of $ThCr_2Si_2$ was conducted by Ivanovskii et al.[4] in 2011. In 1996, Pauer et al.[5] conducted a comprehensive geometric analysis of ≈600 compounds with the $ThCr_2Si_2$-type configuration. In 1989, Venturini et al.[6] developed the lattice parameters and internal coordinates of $CaRh_2Ge_2$ and YRh_2Ge_2. Later, the crystal structure of $SrRh_2Ge_2$ and $BaRh_2Ge_2$ was optimized by Gonzalez et al.[7] in 1993. The iron-based superconductors AFe_2As_2 (A = Ca, Ba, Sr, Eu) with critical temperature T_c (up to 49 K) were discovered in 2008, which belong to the $ThCr_2Si_2$-type structure and play a vital role in modern technology.[8–10] However, due to the manufacturing difficulty

M. A. Rahman, M. Zugrufa
Department of Physics
Pabna University of Science and Technology
Pabna 6600, Bangladesh
E-mail: atikphy@pust.ac.bd

M. A. Khatun
Department of Physics
Hajee Mohammad Danesh Science and Technology University
Dinajpur 5200, Bangladesh

M. H. Mia
Department of Textile Engineering
Uttara University
Uttara-16, Dhaka 1230, Bangladesh

A. Irfan
Department of Chemistry
College of Science
King Khalid University
Abha 61413, Saudi Arabia

The ORCID identification number(s) for the author(s) of this article can be found under https://doi.org/10.1002/pssb.202400230.

DOI: 10.1002/pssb.202400230

of Fe-based materials, researchers have tried to find alternative materials. After that, various superconducting materials with low critical temperatures have been synthesized. Some examples of these superconductors are: YPd_2Si_2 as well as YRh_2Si_2[11] having $T_c < 3$ K; $BaNi_2P_2$ ($T_c = 2.80$ K), $BaIr_2P_2$ ($T_c = 1.97$ K), $BaRh_2P_2$ ($T_c = 0.70$ K);[12] YPt_2Si_2;[13] YIr_2Si_2 ($T_c = 2.52$ K);[14] $SrIr_2Ge_2$, $SrNi_2Ge_2$ ($T_c < 1.8$ K),[15] and $CaPd_2Ge_2$ ($T_c = 1.98$ K),[16] $CaPd_2As_2$ ($T_c = 1.27$ K),[17] $SrPd_2Ge_2$ ($T_c = 3.04$ K).[18]

Maple et al.[19] and Marazza et al.[20] have examined the superconducting behaviour of URu_2Si_2 with a critical temperature (T_c) of 1.5 K and experimentally synthesized the compounds URh_2Si_2 and UPd_2Si_2. They mentioned that, these compounds have ternary layered $ThCr_2Si_2$-type tetragonal configuration and offer intriguing prospects for technological applications. A lot of theoretical works of $ThCr_2Si_2$-type ternary intermetallic compounds are found in literature. Very recently, Parvin et al. studied the structural, mechanical, optical, electronic, and thermal features of layered $BaPd_2As_2$ superconductor.[21] Gui et al.[22] investigated the structural, electronic, and magnetic properties of Monoclinic 122-Type $BaIr_2Ge_2$ in 2017. Salma et al. examined the physical features of 122-type Rh-based materials ARh_2Ge_2 (A = Ca, Sr, Y, and Ba) through density functional theory (DFT) simulation and mentioned the significance applications of these compounds in TBC materials.[23] In 2018, Ciesielski et al. synthesized the materials $LaTE_2Ge_2$ (TE = Fe, Co, Ni, Cu, and Ru) by Rietveld refinement and investigated the electronic features of these materials.[24] Very recently, we have studied about the structural aspects, mechanical, and electronic manner, as well as optical and thermodynamic features of the superconducting disilicide YT_2Si_2 (T = Co, Ni, Ru, Rh, Pd, Ir) and La-based superconductors LaM_2Si_2 (M = Co, Cu, Rh, Pd, Ag, Ir, Pt, Au) by ab initio methods.[25,26] Though a lots of hypothetical works on 122-type intermetallic compounds have been available in literature, but there still missing about the physical properties of U-based materials.

Therefore, in this research paper, a comprehensive theoretical exploration of the structural, mechanical, electronic, thermal, as well as optical properties of UT_2Si_2 (T = Ru, Rh, and Pd) has been carried out through DFT simulation utilizing the CASTEP code. Especially, the lack of theoretical and experimental investigations into the elastic properties of UT_2Si_2 (T = Ru, Rh, and Pd) compounds is particularly noteworthy. Elastic constants, which offer insights into binding properties, anisotropic bonding nature, structural stability, and material stiffness, are crucial for understanding the mechanical behavior of materials. Therefore, our research endeavors to address this gap by conducting an extensive theoretical investigation into the structural, mechanical, and electronic properties of U-based 122-type intermetallic compounds UT_2Si_2 (T = Ru, Rh, and Pd). By comprehensively studying these physical characteristics, we seek to unlock the full potential of these compounds in various technological applications.

2. Computational Details

The investigation into the physical belongings of UT_2Si_2 (T = Ru, Rh, and Pd) was conducted through a first-principles routine utilizing the DFT framework. The computations were facilitated by the pseudo-potential plane-waves method implemented in the CASTEP code.[27,28] The energy of the exchange-correlation functional was evaluated using the GGA estimation in concurrence with the Perdew–Burke–Ernzerhof (PBE)[29] functional. Interactions between electrons and ions were described using Vanderbilt-type ultrasoft pseudo potentials.[30] For sampling the Brillouin-zone adequately, Monkhorst–Pack gridspoint[31] of specific dimensions were employed for each compound: $17 \times 17 \times 7$ for URu_2Si_2, $15 \times 15 \times 6$ for URh_2Si_2, and $16 \times 16 \times 6$ for UPd_2Si_2. Plane wave cut-off energy of 470 eV was selected for this calculation. Geometry optimization was performed using the BFGS[32] (Broyden–Fletcher–Goldfarb–Shanno) relaxation method to determine the ground state of each phase. The optimization criteria included an energy convergence threshold of 5.0×10^{-6} eV atom^{-1}, a maximum force tolerance of 0.01 eV Å^{-1}, a maximum stress limit of 0.02 GPa, and a maximum displacement criterion of 5.0×10^{-4} Å, ensuring ultra-fine quality convergence. Elastic stiffness constants were computed at the optimized structures using the finite stress–strain technique[33] according to Hooke's law. The ELATE code[34] was employed to explore anisotropy nature by 3D contours. Furthermore, the CASTEP code was utilized directly to observe the photon-associated optical characteristics of UT_2Si_2 (T = Ru, Rh, and Pd) compounds.

3. Results and Discussion

3.1. Structural Belongings of UT_2Si_2 (where T = Ru, Rh, and Pd)

At ambient temperature and pressure, the compounds UT_2Si_2 (T = Ru, Rh, and Pd) belong to tetragonal crystal structures reminiscent of the $ThCr_2Si_2$ type, characterized by the space group of $I4/mmm$ (No. 139).[35] The standard and optimized unit cell structures of UT_2Si_2 (where T = Ru, Rh, and Pd) are depicted in **Figure 1**a,b. Each unit cell comprises two formula units, containing 10 atoms, indicating that a single primitive cell contains one formula unit composed of five atoms. In the unit cell of the titled compounds, the U atom occupies the 2a position at coordinates (0, 0, 0). At the 4d sites with coordinates (0, 0.5, 0.25), the Ru/Rh/Pd atoms are located, while the Si atom is located at the 4e sites with coordinates (0, 0, z_{Si}), where "z_{Si}" denotes the internal parameter. **Table 1** presents the optimized lattice parameters a, c, and the equilibrium cell volume V of UT_2Si_2 (T = Ru, Rh, and Pd) alongside with available data. It includes synthesized lattice parameters, cell volumes, Wyckoff positions post-optimization, atomic positions, and unit cell dimensions. The examined structural parameters are closely matched with the experimental data, affirming the precision of the current simulations.

Although the titled compounds UT_2Si_2 (T = Ru, Rh, and Pd) have been successfully synthesized experimentally, we have also calculated the cohesive energy of the compounds to ensure their thermodynamic stability and to ensure the reliability of this research. Negative cohesive energy implies chemical/thermodynamical stability of a compound. In the case of UT_2Si_2 (T = Ru, Rh, and Pd), the cohesive energy can be evaluated using the following expression:[36–38]

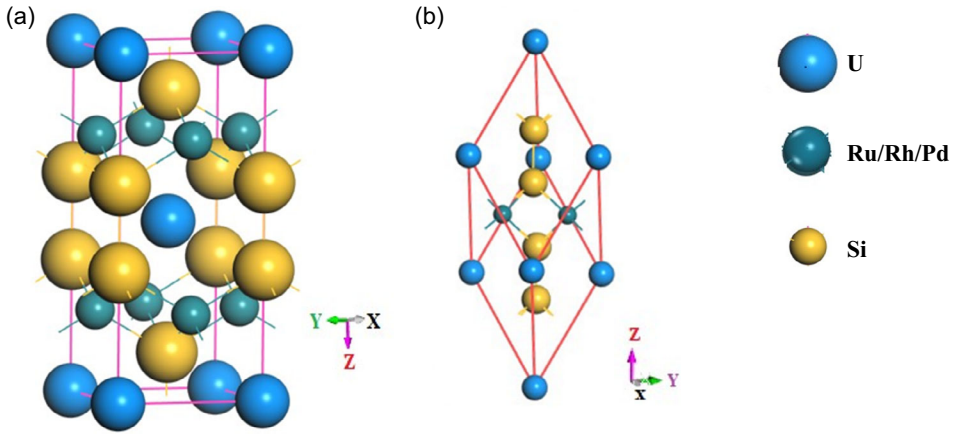

Figure 1. The crystal structure of UT_2Si_2 (T = Ru, Rh, and Pd); a) Conventional unit cell (3D) and b) Primitive unit cell (3D).

Table 1. The equilibrium lattice constants a and c (in Å) along with the cell volume V (in Å^3) for the superconducting polymorphs of UT_2Si_2 (T = Ru, Rh, and Pd).

Compounds	$a=b$	c	$V=a^2c$	E_{coh} [eV atom^{-1}]	Atomic positions[8]					References
					Wyckoff	Element	x	y	z	
URu_2Si_2	4.099	9.459	158.901	−1.011	2a	U	0	0	0	This study
					4d	Ru	0	0.5	0.25	
					4e	Si	0	0	0.368	
	4.129	9.575								Expt.[19]
URh_2Si_2	4.000	9.977	159.763	−1.063	2a	U	0	0	0	This study
					4d	Rh	0	0.5	0.25	
					4e	Si	0	0	0.378	
	4.009	10.025								Expt.[20]
UPd_2Si_2	3.994	10.235	163.240	−1.007	2a	U	0	0	0	This study
					4d	Pd	0	0.5	0.25	
					4e	Si	0	0	0.383	
	4.089	10.051								Expt.[20]

$$E_{coh} = \frac{E_{tot}(UT_lSi_n) - E_U - lE_T - nE_{Si}}{N} < 0 \quad (1)$$

where, $E_{tot}(UT_lSi_n)$ is the total energy, E_U, E_T, and E_{Si} are the energies of U, T (Ru/Rh/Pd), and Si, respectively. The coefficients l, m, and n represent the number of individual atoms, and N is the total number of atoms per unit cell. The calculated negative values of E_{coh} indicate phase stability of UT_2Si_2 (T = Ru, Rh, and Pd) and ensures the reliability of this simulation.

We have utilized the Birch–Murnaghan equation of state (EOS) to investigate how the total energy (E) of the UT_2Si_2 (where T = Ru, Rh, and Pd) varies with the change in their unit cell volume (V) by fitting the calculated total energy data as a function of unit cell volume. This analysis aimed to predict the stability of these compounds under different volumes and pressures. The calculated Birch–Murnaghan equation of states (EOS) is defined as follows:[39,40]

$$E(V) = E_0 + \frac{9V_0B_0}{16}\left\{\left[\left(\frac{V_0}{V}\right)^{2/3} - 1\right]^3 B_0' + \left[\left(\frac{V_0}{V}\right)^{2/3} - 1\right]^2\left[6 - 4\left(\frac{V_0}{V}\right)^{2/3}\right]\right\} \quad (2)$$

where E_0 is the total energy corresponding to the equilibrium unit cell volume V_0, B_0 is the bulk modulus, and B_0' is the pressure derivative of the bulk modulus. From the figures presented in the paper (**Figure 2**a–c), it is evident that URu_2Si_2 exhibits a more stable structure compared to URh_2Si_2 and UPd_2Si_2, as indicated by its larger negative value of ground-state energy. Additionally, the equilibrium volume, where the energy of the

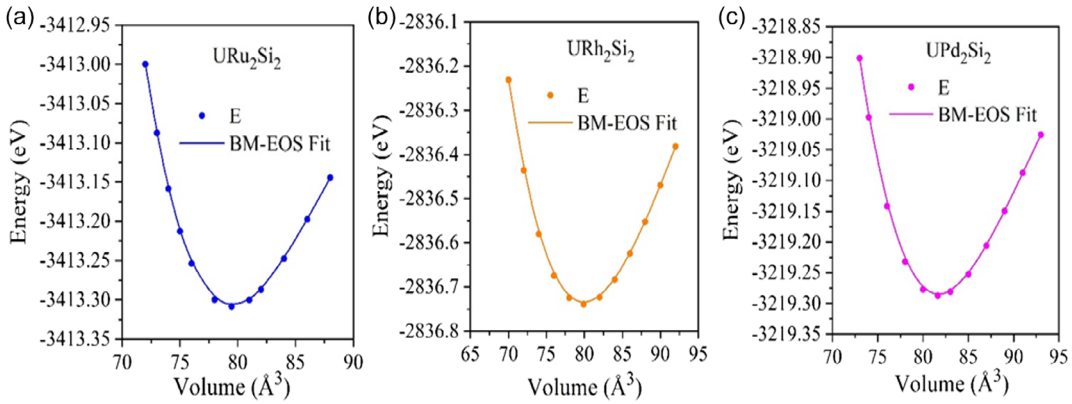

Figure 2. The relationship between total energy and unit cell volume for a) URu_2Si_2, b) URh_2Si_2, and c) UPd_2Si_2 during structural optimization.

unit cell reaches its lowest point, is an important parameter for computing the ground state energy.

3.2. Mechanical Characteristics

The elastic constants provide the fundamental material's parameters that offer a comprehensive insight into the mechanical and dynamic behavior of solid materials. They play a vital role in understanding the ductility, breakability, mechanical constancy, anisotropy, and stiffness of solids.[41] The mechanical properties included the independent elastic constants and dependent polycrystalline parameters. The elastic constants are calculated by the finite stress–strain method according to Hooke's law. Since, UT_2Si_2 (T = Ru, Rh, and Pd) exhibits tetragonal crystal structure, for this reason all phases have six independent elastic constants, i.e., C_{11}, C_{12}, C_{13}, C_{33}, C_{44}, and C_{66}. Stiffness parameters should contain positive values and remain obligatory to fulfill the following mechanical stability conditions called the Born' criteria[42] for the structure of tetragonal crystal:

$$\left.\begin{aligned} &C_{11} > 0, \quad C_{44} > 0, \quad C_{33} > 0, \quad C_{66} > 0 \\ &C_{11} - |C_{12}| > 0 \\ &C_{11} + C_{33} - 2C_{13} > 0 \\ &2(C_{11} + C_{12}) + C_{33} + 4C_{13} > 0 \end{aligned}\right\} \tag{3}$$

Table 2 represents the elastic constants, examined using the stress–strain approach. All of them satisfy the specified conditions, affirming the mechanical stability of UT_2Si_2 (T = Ru, Rh, and Pd) in nature. Since no experimental or other theoretical results on elastic constants are available in literature, for this reason the elastic constants values, C_{ij} of some similar types of compounds are listed also in Table 2 along with the studied compounds UT_2Si_2 (T = Ru, Rh, and Pd).

The material's stiffness alongside *a*-and *c*-crystallographic axis is represented by elastic constants C_{11} and C_{33}.[43] Not only that, these factors also denote the material's ability to resists the linear compression upon stress, whereas the parameters C_{12}, C_{13}, and C_{44} indicate the ability of a material to resist shape deformation.

Table 2. The evaluated elastic constants C_{ij} (in GPa) for UT_2Si_2 (T = Ru, Rh, and Pd).

Compounds	Elastic constants						References
	C_{11}	C_{12}	C_{13}	C_{33}	C_{44}	C_{66}	
URu_2Si_2	272.466	181.281	117.738	356.081	98.752	146.466	This Study
URh_2Si_2	283.532	160.443	135.059	362.335	104.663	155.952	
UPd_2Si_2	238.750	110.186	138.960	264.489	80.628	68.255	
YPd_2Si_2	215.70	67.01	118.47	234.04	75.98	47.79	Remarks[25]
YNi_2Si_2	239.88	54.81	94.01	248.98	97.36	56.81	
YRu_2Si_2	266.88	97.56	93.87	222.26	78.87	114.27	
YRh_2Si_2	256.03	124.66	105.12	257.14	95.59	122.91	
$LaCu_2Si_2$	207.35	46.19	82.65	186.86	99.18	65.36	Remarks[26]
$LaRh_2Si_2$	228.42	119.03	92.29	150.31	91.45	114.01	
$LaPd_2Si_2$	196.99	65.40	97.18	193.65	71.93	46.29	
$LaAg_2Si_2$	177.36	52.84	78.98	173.46	81.09	56.46	
$LaPt_2Si_2$	199.54	63.78	101.54	212.15	78.31	14.85	
$LaAu_2Si_2$	187.99	58.94	96.92	193.46	74.98	42.29	

Also the stiffness parameter C_{44} is directly related to the material's hardness. High value of C_{44} denoted high hardness of a material. Here the large values of elastic stiffness parameters C_{33} than C_{11} ensure that the studied phases have huge ability to resist linear deformation along *c*-axis compared to *a*-axis. However the phase URh_2Si_2 carries the high C33 value compared to others which ensures that this material has high capability to resist linear deformation than URu_2Si_2 and UPd_2Si_2. Not only that, the phase URh_2Si_2 has high C_{44} values compared to URu_2Si_2 and UPd_2Si_2 confirming that it is more harder material than URu_2Si_2 and UPd_2Si_2.

Utilizing the computed elastic constants, the Young's modulus (E), shear modulus (G), bulk modulus (B), Poisson's ratio (ν), B/G values, Vickers hardness (H_v), and universal anisotropy (A^U) for the UT_2Si_2 (where, T = Ru, Rh, and Pd) have been calculated through the Voigt–Reuss–Hill estimations.[44–46] According to these estimations, the shear and bulk moduli for the tetragonal arrangement can be expressed as follows:

$$\left.\begin{aligned} B_V &= (2C_{11} + 2C_{12} + C_{33} + 4C_{13})/9 \\ \text{and } B_R &= C^2/M \end{aligned}\right\} \tag{4}$$

$$\left.\begin{aligned} G_V &= (M + 3C_{11} - 3C_{12} + 12C_{44} + 6C_{66})/30 \\ \text{and } G_R &= 15\Big/\left[\frac{18B_V}{C^2} + \frac{6}{(C_{11} - C_{12})} + \frac{6}{C_{44}} + \frac{3}{C_{66}}\right] \end{aligned}\right\} \tag{5}$$

where, $M = C_{11} + C_{12} + 2C_{33} - 4C_{13}$ and $C^2 = (C_{11} + C_{12})C_{33} - 2C_{13}^2$.

The mean values for the shear modulus (G) and bulk modulus (B) as reported by Hill are determined through the following two relations:

$$\left.\begin{aligned} B &= B_H = (B_R + B_v)/2 \\ \text{and } G &= G_H = (G_R + G_v)/2 \end{aligned}\right\} \tag{6}$$

We can now compute the Poisson's ratio (ν) and Young's modulus (E) using the relations provided below,

$$\left.\begin{aligned} E &= \frac{9GB}{3B + G} \\ \text{and } \nu &= \frac{3B - 2G}{2(3B + G)} \end{aligned}\right\} \tag{7}$$

The crystal's anisotropic properties can be assessed by using the subsequent equation[47]

$$A^U = \frac{5G_V}{G_R} - 6 + \frac{B_V}{B_R} \tag{8}$$

The predictive estimation of material's hardness can be achieved through the utilization of the following relation:[48]

$$H_v = 2(GK^2)^{0.585} - 3 \tag{9}$$

here, $K = G/B$

Utilizing the aforementioned subsequent relations the computed polycrystalline bulk factors of UT_2Si_2 (T = Ru, Rh, and Pd) are listed in **Table 3**. Notably, there is currently no available experimental or theoretical data on polycrystalline elastic constants for these compounds. Surprisingly, several of our computed elastic moduli are closely resemble with the previous studied materials YT_2Si_2 (T = Co, Ni, Ru, Rh, Pd, Ir) and LaM_2Si_2 (M = Co, Cu, Rh, Pd, Ag, Ir, Pt, Au).[25,26] This alignment validates the accuracy of our computational methodology and reinforces the reliability of our findings.

The bulk modulus (B) is a critical parameter in material science and engineering, reflecting a material's resistance to plastic deformation or volume compression. Among the investigated compounds, URh_2Si_2 demonstrates the highest B value, followed by URu_2Si_2, and UPd_2Si_2 (Table 3) which ensures that it has more ability to resist volume deformation compared to others. Not only that, the compound URh_2Si_2 caries the high bulk

Table 3. The calculated polycrystalline properties, including Young's modulus (E in GPa), B/C_{44} values, B/G values, shear modulus (G in GPa), Poisson's ratio (ν), bulk modulus (B in GPa), Vickers hardness ($H_v$in GPa), and elastic anisotropy (A^U) for the UT_2Si_2 compound (T = Ru, Rh, and Pd).

Compounds	B	G	E	B/G	B/C_{44}	ν	A^U	H_v	References
URu_2Si_2	192.44	93.90	242.33	2.049	1.95	0.290	0.828	9.315	This work
URh_2Si_2	198.44	101.83	260.86	1.949	1.89	0.281	0.466	10.69	
UPd_2Si_2	167.67	68.59	181.08	2.444	2.08	0.320	0.146	5.33	
YPd_2Si_2	134.31	80.78	201.88	1.663	1.379	0.249	0.259	11.40	Remarks[26]
YNi_2Si_2	146.81	84.64	212.99	1.735	1.861	0.258	0.145	11.09	
YRu_2Si_2	159.81	89.79	226.88	1.780	1.672	0.263	0.227	11.15	
YRh_2Si_2	139.53	62.16	162.37	2.245	1.836	0.306	0.343	5.70	
$LaCu_2Si_2$	113.74	76.07	186.61	1.50	1.15	0.23	0.37	12.50	Remarks[27]
$LaRh_2Si_2$	130.55	74.56	187.91	1.75	1.43	0.26	0.80	9.94	
$LaPd_2Si_2$	122.67	58.44	151.29	2.10	1.71	0.29	0.26	6.07	
$LaAg_2Si_2$	105.32	63.12	157.83	1.67	1.30	0.24	0.29	9.42	
$LaPt_2Si_2$	126.21	47.96	127.42	2.63	1.61	0.23	2.42	3.20	
$LaAu_2Si_2$	118.59	57.39	148.27	2.07	1.58	0.33	0.41	7.09	

modulus among all the compounds listed in Table 3. The sequence of bulk moduli of the aforementioned compounds is: $URh_2Si_2 > URu_2Si_2 > UPd_2Si_2 > YRu_2Si_2 > YNi_2Si_2 > YRh_2Si_2 > YPd_2Si_2 > LaRh_2Si_2 > LaPt_2Si_2 > LaPd_2Si_2 > LaAu_2Si_2 > LaCu_2Si_2 > LaAg_2Si_2$.

The shear deformation against the external force of a material is represented by shear modulus (G) where the high G value indicates high resistance to shear deformation. Here the studied phases UT_2Si_2 (T = Ru, Rh, and Pd) carry high shear modulus compared to the reference compounds confirming their high ability to shear deformation; whereas the phase URh_2Si_2 exhibits a higher shear modulus (G) compared to the other compounds, indicating its superior ability to withstand shear deformation. The sequence of shear moduli of the aforementioned compounds is: $URh_2Si_2 > URu_2Si_2 > YRu_2Si_2 > YNi_2Si_2 > YPd_2Si_2 > LaCu_2Si_2 > LaRh_2Si_2 > UPd_2Si_2 > LaAg_2Si_2 > YRh_2Si_2 > LaPd_2Si_2 > LaAu_2Si_2 > LaPt_2Si_2$.

On the contrary, the Young's modulus (E) refers the resistance to linear deformation of a material. It is also inversely related to the thermal shock coefficient R, where the lower E value corresponds to greater resistance to thermal shock.[49] In this study, the observed lower Young's modulus (E) value for UPd_2Si_2 indicates its heightened capacity to withstand thermal shock compared to the other compounds investigated. A lower E value implies greater flexibility or deformation capability under stress, making UPd_2Si_2 more capable to resist thermal shock-induced fractures. Thus, the phase UPd_2Si_2 may be considered more suitable for applications requiring resistance to thermal shock, such as in thermal barrier coatings (TBC), compared to the other studied compounds. But considering all compounds listed in Table 3, it is very obvious that the phase $LaPt_2Si_2$ carries the lowest Young's modulus compared to all materials, which ensures that it is more suitable for using in TBC materials. Conversely, the material URh_2Si_2 carries the maximum values of Young's modulus among all the materials listed in Table 3, approving that the phase URh_2Si_2 is more capable of repelling the linear deformation. According to the calculated values the sequence of Young's moduli of the listed compounds is: $URh_2Si_2 > URu_2Si_2 > YRu_2Si_2 > YNi_2Si_2 > YPd_2Si_2 > LaRh_2Si_2 > LaCu_2Si_2 > UPd_2Si_2 > YRh_2Si_2 > LaAg_2Si_2 > > LaPd_2Si_2 > LaAu_2Si_2 > LaPt_2Si_2$.

To anticipate whether a material displays ductile or brittle characteristics, scientist Pugh formulated a formula that incorporates the ratio of bulk modulus to shear modulus, denoted as (B/G). A material is characterized as ductile if the B/G ratio is above 1.75; otherwise, it is identified as brittle.[50] The Poisson's ratio, denoted as ν, is another essential bulk parameter that predicts a material's ductile or brittle nature. According to the criterion established,[51] a material exhibits ductile behavior when $\nu > 0.26$ and brittle nature when $\nu < 0.26$. Based on this criterion, the investigated compounds URu_2Si_2, URh_2Si_2 and UPd_2Si_2 demonstrate a ductile nature, as indicated in Table 3.

In the context of industrial manufacturing, the machinability index (μ) serves as a critical metric for evaluating the efficiency and cost-effectiveness of production processes. This index denoted by μ, is influenced by various factors such as cutting geometry, cutting type, rigidity, hardness, and the capabilities of machine tools.[52] It is defined as the ratio between the bulk modulus (B) and the shear resistance (C_{44}), as expressed[53]

$$\mu = B/C_{44} \tag{10}$$

The machinability index serves as a valuable indicator for evaluating not only the ease of machining but also the lubricating properties and plasticity of a material.[54–56] Higher B/C_{44} values suggest enhanced lubrication, reduced friction, and increased plastic deformation capability. According to our analysis, it is observed that the studied phases UT_2Si_2 (T = Ru, Rh, and Pd) have higher machinability compared to the reference compounds which ensure that these phases are more machinable and can be used for industrial purposes. However, the phase UPd_2Si_2 exhibits a high machinability index compared to all materials (Table 3), indicating superior machinability. Interestingly, despite having lower bulk modulus, Young's modulus, and shear moduli values, materials like UPd_2Si_2 can still demonstrate exceptional machinability. This characteristic renders them promising choices for various industrial applications, highlighting the significance of machinability in material selection and process optimization. According to the values of B/C_{44} the sequence of machinable index is: $UPd_2Si_2 > URu_2Si_2 > URh_2Si_2 > YNi_2Si_2 > YRh_2Si_2 > LaPd_2Si_2 > YRu_2Si_2 > LaAg_2Si_2 > LaAu_2Si_2 > LaRh_2Si_2 > YPd_2Si_2 > LaAg_2Si_2 > LaCu_2Si_2$.

In practical applications of solid materials, the understanding of their anisotropic nature is very crucial. Mechanical anisotropy significantly influences various physical phenomena, such as anisotropic plastic deformation, crack behavior, and phonon modes.[57] A material is deemed completely isotropic when A^U equals zero; any deviation from zero indicates anisotropic behavior. According to the values of A^U as shown in Table 3, the anisotropic nature of UT_2Si_2 (T = Ru, Rh, and Pd) is ensured.

Hardness is a crucial macroscopic property of materials with varied industrial and technological applications. Materials with high hardness display greater resistance to plastic deformation, making them ideal for machining. Optimal machinability[58] and damage tolerance are often associated with hardness values falling within the range of 2–8. From the analysis of Table 3 it is ensured that the phase URh_2Si_2 exhibits the highest hardness (since it carries a high Young's modulus) among the three studied compounds, indicating its superior resistance to plastic deformation compared to the others. Conversely, the lower hardness of UPd_2Si_2 suggests its greater machinability relative to the other compounds under investigation.

The visual representation of Young's modulus, shear modulus, and Poisson's ratio in various crystal planes are measured utilizing the ELATE open access code.[34] The three-dimensional (3D) shapes depicted in **Figure 3** emphasize the materials' anisotropic characteristics. Here the deep green color over the solid represents the maximum anisotropy in the Young's modulus where the clouds with deep blue color denotes the maximum anisotropy in the shear modulus and Poisson's ratio. In the case of isotropic solids, the anticipated 3D plots for these elastic parameters would form perfect spheres; any deviation from this spherical shape indicates anisotropy. As observed in Figure 3a and **Table 4**, URu_2Si_2 exhibits a higher degree of anisotropy compared to URh_2Si_2 and UPd_2Si_2. Maximum anisotropy is found in the case of Poisson's ratio for all the compounds.

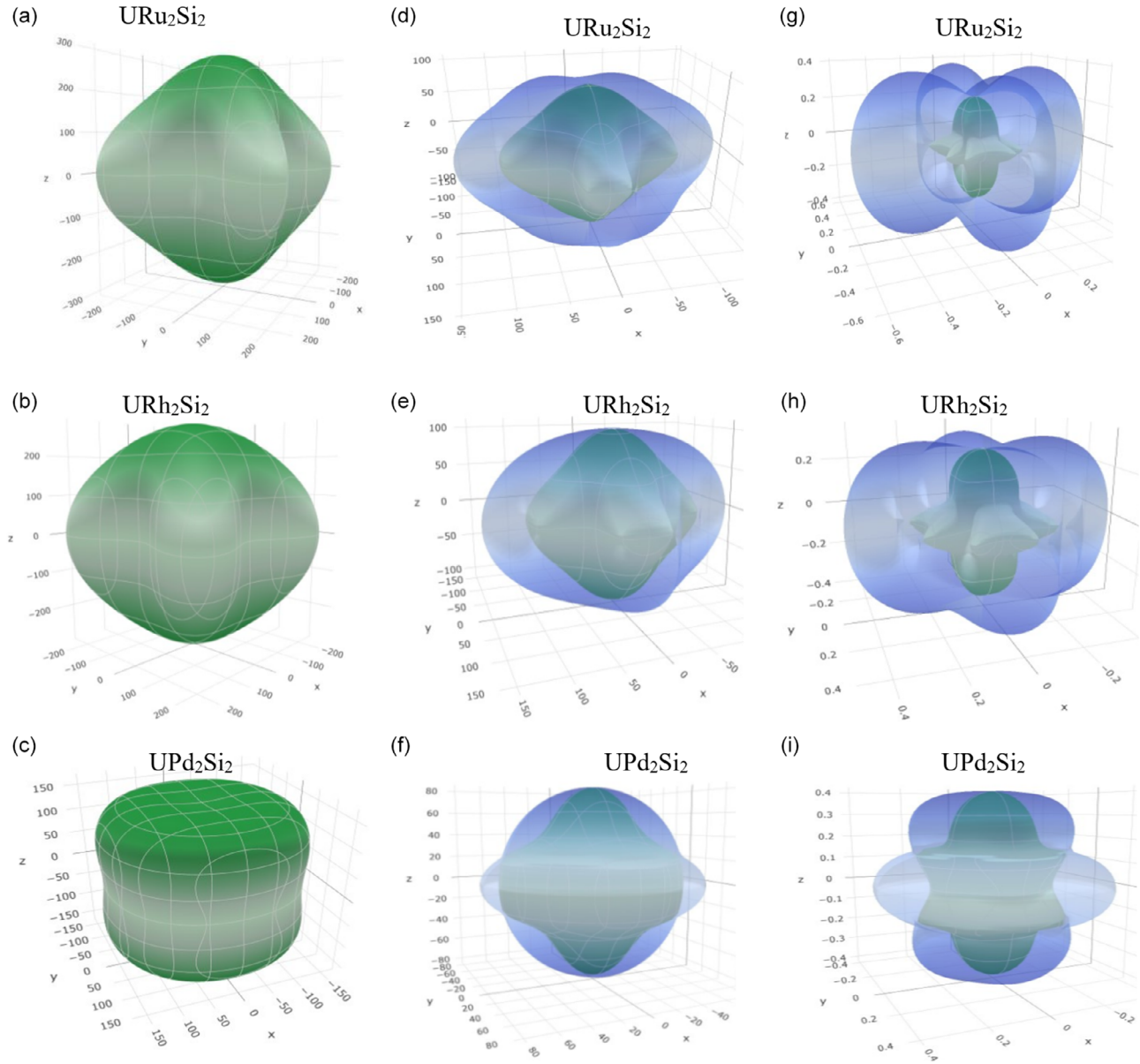

Figure 3. 3D plots of a–c) Young's modulus, d–f) Shear modulus, g–i) Poisson's ratio of UT_2Si_2 (T = Ru, Rh, and Pd).

Table 4. The lowest and highest values of Young's modulus, E (in GPa), shear modulus, G (in GPa), and Poisson's ratio for UT_2Si_2 (T = Ru, Rh, and Pd).

Compounds	E_{min}	E_{max}	A_Y	G_{min}	G_{max}	A_G	ν_{min}	ν_{max}	A_ν
URu_2Si_2	146.77	329.26	2.24	45.59	146.47	3.21	0.09	0.61	6.95
URh_2Si_2	181.21	329.26	1.80	61.55	155.95	2.53	0.05	0.48	9.91
UPd_2Si_2	153.81	201.75	1.31	55.45	80.626	1.45	0.19	0.41	2.17

3.3. Electronic Behaviors and Bonding Nature

We have extensively examined the electronic band structure, as well as the partial and total density of states, utilizing the Mulliken atomic population and the overall charge density of UT_2Si_2 (T = Ru, Rh, and Pd) for a comprehensive understanding of the electronic properties and chemical bonding exist in these compounds. **Figure 4** illustrates the electronic band structures of UT_2Si_2 (T = Ru, Rh, and Pd) along the highly symmetric path (Z-A-M-G-Z-R-X-G) across the Brillouin zone, encompassing the energy range from −2 to 2 eV. The Fermi Level (E_F) is designated by the horizontal scattered line in the middle of the valence and conduction band. Figure 4a–c clearly illustrates the overlapping of different valence bands with the conduction bands around the Fermi level, indicating the absence of a band gap. This investigation confirms that the compounds UT_2Si_2 (T = Ru, Rh, and Pd) exhibit metallic character.

The metallic properties observed in the compound UT_2Si_2 (T = Ru, Rh, and Pd) can be ascribed to the combined influences

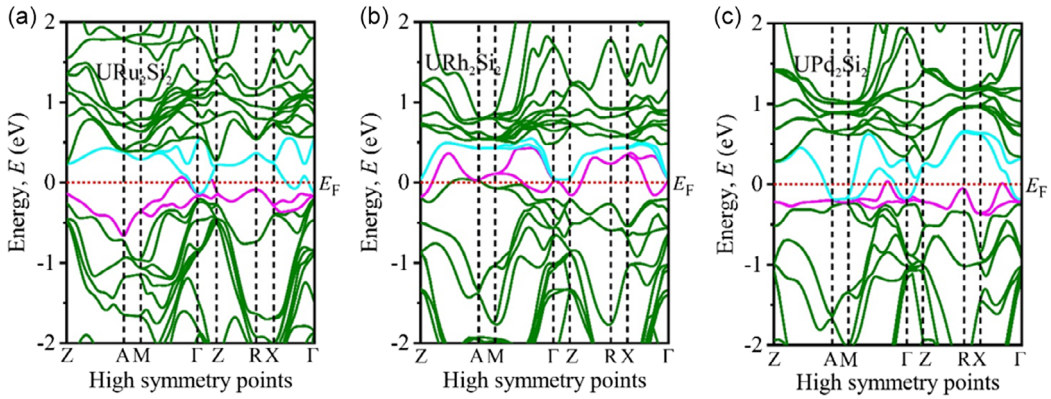

Figure 4. The electronic band structures of UT_2Si_2 (T = Ru, Rh, and Pd) along the high-symmetry direction in the Brillouin zone.

of partial and total density of states (TDOS) at the Fermi level. **Figure 5**a–c presents the DOS (both total and partial) for all phases, covering an energy range from −15 to 15 eV. The dotted line at 0 eV specifies the Fermi level, E_F distinguishing between the valence bands and the conduction bands. Below the Fermi level, a prominent peak is observed in all phases at ≈−4 eV, primarily originated from the robust hybridization of Ru-4*d*, Rh-4*d*, Pd-4*d*, and Si-3*p* states. This highlighted the covalent bonding between Ru—Si, Rh—Si, and Pd—Si. The primary source of density of states at the Fermi level is attributed for the Ru-4*d*, Rh-4*d*, and Pd-4*d* states for compounds URu_2Si_2, URh_2Si_2, and UPd_2Si_2 respectively. This is visually represented in Figure 5a–c. The conduction bands are mainly originated from U-6*d*, Ru-4*d*, Si-3*p* states for URu_2Si_2; U-6*d*, Rh-4*d*, Si-3*p* states for URh_2Si_2, and U-6*d*, Pd-4*d*, Si-3*p* states for UPd_2Si_2. The graphical depiction of the TDOS for the three examined compounds is presented in Figure 4a–c. It is evident from the figure that at the Fermi level, the TDOS for UPd_2Si_2 is higher than that of URu_2Si_2 and URh_2Si_2.

It is noteworthy that the electrical stability of a compound is best maintained when $N(E_F)$ is kept at a lower value rather than a higher value.[59] This is because a lower $N(E_F)$ implies a narrower band of available electronic states at the Fermi level, which in turn signifies a more stable electronic configuration. In contrast, a higher $N(E_F)$ could potentially lead to a broader band of electronic states at the Fermi level, increasing the likelihood of electronic instabilities and contributing to a less stable electronic structure. The DOS for URu_2Si_2, URh_2Si_2, and UPd_2Si_2 at the Fermi level is ≈6.70, ≈12.78, and ≈8.27 eV/states, respectively. These values reflect the density of electronic states available at the Fermi level for each compound.

To deepen our understanding about the charge distribution and bonding characteristics within UT_2Si_2 (T = Ru, Rh, and Pd), we have computed the charge density and Mulliken atomic

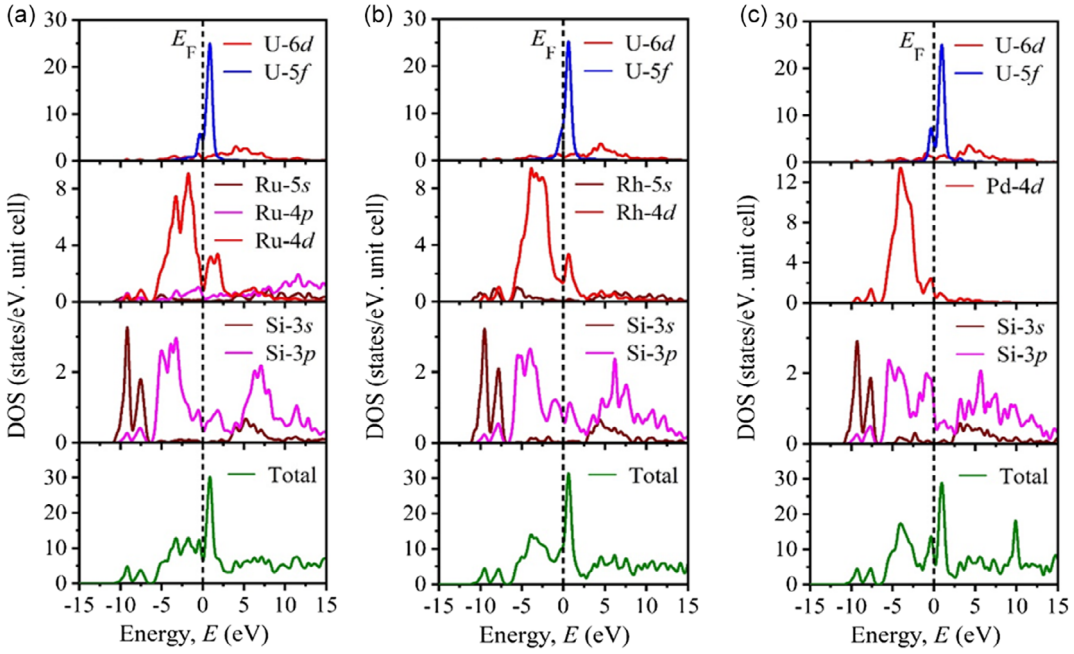

Figure 5. Total and partial electronic DOS of a) URu_2Si_2, b) URh_2Si_2, and c) UPd_2Si_2.

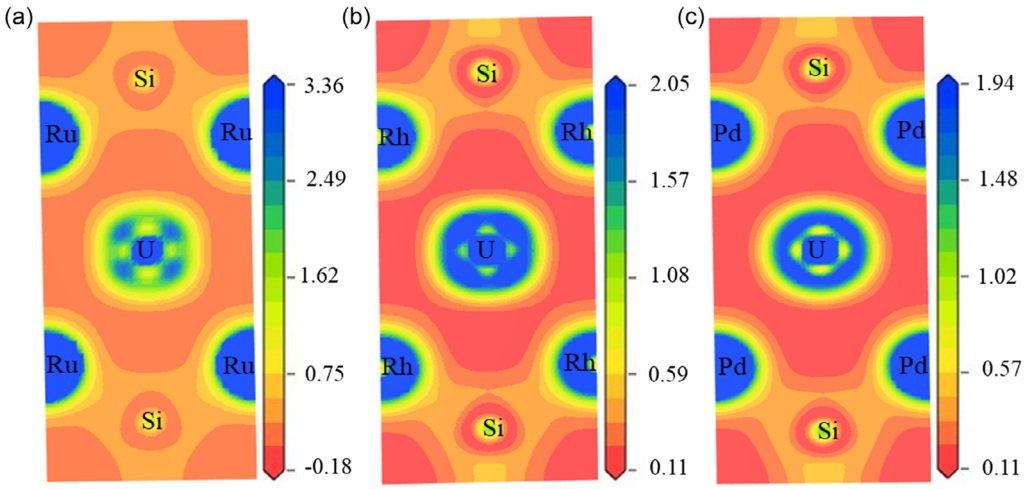

Figure 6. Charge density map of a) URu_2Si_2, b) URh_2Si_2, and c) UPd_2Si_2.

population,[60–62] as presented in **Figure 6** and **Table 5**. Analysis of Table 5 reveals that Ru, Rh, and Pd atoms carry negative charges in all phases, while U and Si atoms possess positive charges in URu_2Si_2, URh_2Si_2, and UPd_2Si_2, respectively. This suggests a transfer of charge from U, Si atoms to Ru/Rh/Pd for URu_2Si_2, URh_2Si_2, and UPd_2Si_2, respectively. Furthermore, from Figure 6, it is evident that the U—Ru, U—Rh, and U—Pd bonds within URu_2Si_2, URh_2Si_2, and UPd_2Si_2, respectively, exhibit a typically ionic nature. This is indicated by the lack of significant bonding charge to link the Si and Ru/Rh/Pd atoms, resulting in a nearly spherically symmetric charge distribution around each atom. Moreover, the metallic character of the compounds contributes to the ionic nature of the T—T bonds,[63] particularly observed in the Rh—Rh and Pd—Pd bonds. This indicates that the compounds UT_2Si_2 (where, T = Ru, Rh, and Pd) exhibit metallic characteristics, with the ionic character being a consequence of their metallic nature.

The presence of a covalent nature is evident in Si—Ru, Si—Rh, and Si—Pd bonds within URu_2Si_2, URh_2Si_2, and UPd_2Si_2, respectively, characterized by a significant overlap in electron (charge) distribution among these atoms. In contrast, the materials exhibit ionic bonds due to the low value of the bond population. A bond population value of zero indicates a perfectly ionic bond, whereas a higher value suggests a covalent bond, with the degree of covalency increasing with increasing the bond population. The bonding and antibonding states are distinguished by positive and negative bond overlap populations respectively.[64] Analysis of the calculated bond population reveals that the Si—Rh bond in URh_2Si_2 exhibits slightly more covalency compared to the Si—Pd and Si—Ru bonds in UPd_2Si_2 and URu_2Si_2, respectively.

Moreover, negative populations in bonds between two U atoms in UT_2Si_2 (T = Ru, Rh, and Pd) result from the antibonding nature of the p orbitals of the U atoms, as indicated in Table 5. Therefore, a thorough analysis of the DOS, Mulliken atomic population, and total charge density for UT_2Si_2 (where, T = Ru, Rh, and Pd) reveals the coexistence of ionic, covalent, and metallic bonds within these compounds. This observation aligns with the characteristic features of $ThCr_2Si_2$-type compounds.[65]

3.4. Optical Properties

In this sector, we have explored how the optical properties of solids contribute to understanding the electronic arrangement

Table 5. The Mulliken atomic populations of compounds URu_2Si_2, URh_2Si_2, and UPd_2Si_2.

Compounds	Species	*s*	*p*	*d*	Total	Charge	Bond	Population	References
URu_2Si_2	U	2.24	5.62	2.37	10.23	1.01	Ru-Ru	−1.22	This study
	Ru	2.48	6.90	7.28	16.66	−0.66	Si-Ru	0.73	
	Si	4.24	2.61	0.00	3.85	0.15	Si-Si	0.42	
URh_2Si_2	U	2.64	4.90	2.51	10.05	1.19	Rh-Rh	−1.23	
	Rh	0.98	0.37	8.26	9.61	−0.61	Si-Rh	1.04	
	Si	1.34	2.65	0.00	3.99	0.01	Si-Si	0.62	
UPd_2Si_2	U	2.15	5.23	2.46	9.84	1.41	Pd-Pd	−1.02	
	Pd	2.59	0.93	9.31	10.83	−0.83	Si-Pd	1.03	
	Si	1.22	2.65	0.00	3.87	0.13	Si-Si	0.70	

within materials. The research delved into the optical properties of UT_2Si_2 (T = Ru, Rh, and Pd) using various photon energies, examining the complex nature of dielectric function $\varepsilon(\omega) = \varepsilon_1(\omega) + i\varepsilon_2(\omega)$ which varies with frequency, primarily influenced by the electronic setup. In this context, $\varepsilon_1(\omega)$ and $\varepsilon_2(\omega)$ denote the real and imaginary components of the dielectric function, respectively. The value of $\varepsilon_1(\omega)$ may be determined by performing a calculation using the Kramers–Kronig relation:[66]

$$\varepsilon_1(\omega) = 1 + \frac{2}{\pi} P \int_0^{\infty} \frac{\omega' \varepsilon_2(\omega')}{\omega'^2 - \omega^2} d\omega' \tag{11}$$

Understanding the imaginary component, $\varepsilon_2(\omega)$ of the dielectric function we have required to consider the momentum matrix and the various potential transitions between occupied and unoccupied electronic states:[66,67]

$$\varepsilon_2(\omega) = \frac{2e^2\pi}{\Omega\varepsilon_0} \sum_{K,V,C} \left| \langle \psi_k^c | \hat{U}.\vec{r} | \psi_k^V \rangle \right|^2 \delta(E_K^C - E_K^V - E) \tag{12}$$

where, e indicates the electronic charge, the vector that signifies the polarization of the incoming electric field is denoted by $\hat{u}$, Ψ_k^v, and Ψ_k^c represent the wave functions corresponding to the valence band and conduction band at wave vector k in some respects.

The absorption coefficient (α) is an essential parameter that measures the amount of light with a particular energy (wavelength) when it penetrates a substance before getting absorbed. Material's absorption properties offer insights into the efficiency of converting solar energy. In **Figure 7**a, the absorption spectra of UT_2Si_2 (T = Ru, Rh, Pd) are depicted, commencing from 0 eV, attributed to the metallic nature of these materials. As depicted in Figure 7a, across all these compounds, the absorption curve exhibits a similar pattern, showcasing multiple absorption peaks at different energy levels. Nevertheless, each of these compounds exhibits a favorable absorption coefficient. The highest peaks have been found at 24 eV, and at this point, URu_2Si_2, URh_2Si_2 have relatively the same values 3.53×10^4 and $3.58 \times 10^4\,cm^{-1}$, respectively, and UPd_2Si_2 have a low value of about $2.98 \times 10^4\,cm^{-1}$. Since more than 43% of the sun's energy is visible light, this finding will help improve solar cells' performance. The compounds under consideration have potential use as anti-reflection coatings, UV detectors, and other appropriate optoelectronic devices since their largest peaks are seen in the UV energy area.[68]

The correlation between optical conductivity and optical absorption is due to the liberation of free carriers for conduction when the material absorbs photons. A material's conductivity (σ) denotes its capacity to carry electrons based on changes in photon energy.[69] This assists in determining whether the material will exhibit properties of a conductor, semiconductor, or superconductor. The spectrum (Figure 7b) exhibits a similar pattern to the absorption coefficient in Figure 7a since more excellent absorption leads to more conduction. Figure 7b displays that the photoconductivity begins at zero energy, which indicates that the materials have no energy band gap, as evident from the band structure.

The investigation of reflectivity is required to understand the surface properties of UT2Si2 (T = Ru, Rh, Pd) phases.

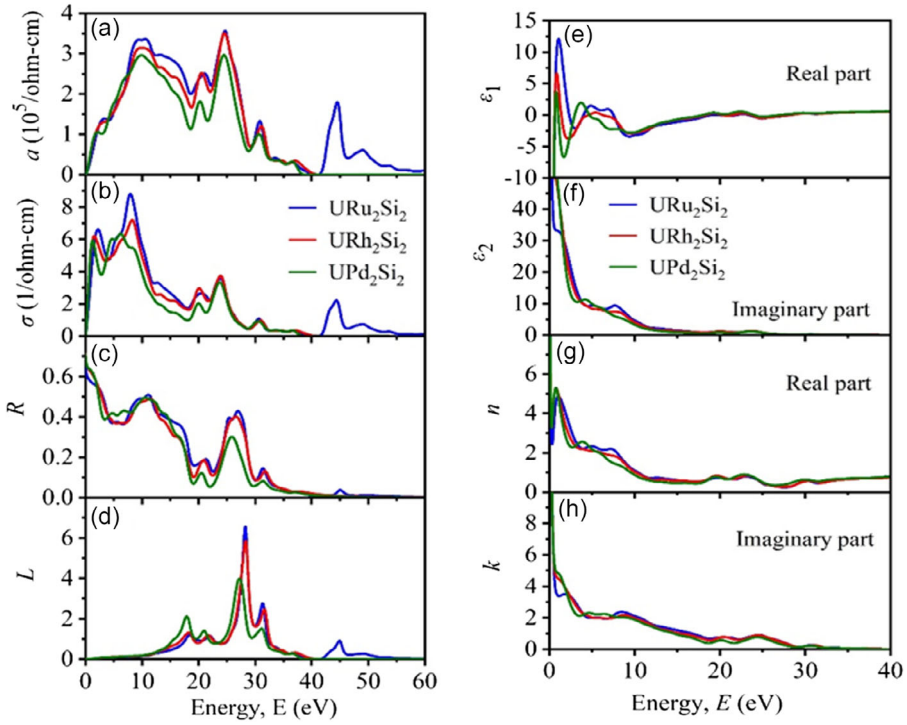

Figure 7. Energy-dependent optical functions a) absorption coefficient, b) conductivity, c) reflectivity, d) loss function, e) real component of dielectric function, f) imaginary component of dielectric function, g) real component of refractive index, and h) imaginary component of refractive index of UT_2Si_2 (T = Ru, Rh, Pd) compounds.

Figure 7c reveals the high reflectivity with values of 6.01–6.08 at zero photon energy. The higher reflection of light at lower energy site refers to the high conductivity and low absorption ability of the studied materials. At the visible site, the average reflectivity of UT_2Si_2 (T = Ru, Rh, Pd) is more than 40%, which confirms that these materials are suitable for using as coating materials for reducing solar heating. Some intense peaks are also appeared between 9.5 and 11.4 eV, suggesting that these phases also reflect the incident light in the UV energy region. As energy increases, both the absorption coefficient and reflectivity progressively diminish.

There exists a strong correlation between the loss function and the dielectric function. The energy loss function (L) is employed to elucidate the optical dielectric framework. It characterizes the energy dissipated by a swift electron while moving through the material.[71] There exists an inverse relationship between the imaginary component of the dielectric function and the loss function. In Figure 7d, it is seen that there is an absence of a notable peak for UT_2Si_2 (T = Ru, Rh, Pd) phases across the photon energy range of 0–12 eV. However, within this area, substantial spectra for all phases are observed for the dielectric imaginary portion, as shown in Figure 7f. The amplitude of the energy loss function, which is referred to as the plasma frequency, seems enormous because the imaginary component of the dielectric function is tiny beyond around 12 eV. When the bounced frequency of light exceeds the plasma frequency, the material transitions from metallic to dielectric characteristics and turns translucent is observed.[72]

Conductivity may also be linked to the dielectric function (Figure 7e,f). The conductivity reaches its maximum value when the real component of the dielectric constant is negative, as seen in Figure 7e. The considerable negative value of $\varepsilon_1(\omega)$ within these phases indicates metallic behavior reminiscent of Drude-like characteristics. Furthermore, the crossing of zero from below for both $\varepsilon_1(\omega)$ and $\varepsilon_2(\omega)$ is indicative of the metallic nature, resembling Drude-like characteristics.[70] For these analyses, we utilized a plasma frequency of 4 eV, along with the utilization of a damping (relaxation) energy set at 0.05 eV. Around 15 eV, or in the UV ranges, the dielectric value becomes zero, and absorption, conductivity, and reflectivity drop in this region. On the contrary, loss function peaks are high in this energy region.

The amount of light that is absorbed by a substance as it passes through it is directly proportional to its refractive index.[73] Additionally, the refractive index is associated with the covalent bonding characteristics of a molecule. Covalently bonded compounds typically exhibit a higher refractive index compared to ionic bonded compounds. In Figure 7g, the static refractive index ($n(0)$) for UT_2Si_2 (T = Ru, Rh, Pd) is depicted, showing a value of ≈112. This high value of refractive index indicates that these materials possess significant potential for enhancing the visual quality of electronic displays such as liquid-crystal display (LCDs) and quantum dot TVs, etc. The static refractive index, $n(0)$, represents the speed of light in a vacuum compared to its speed within the material, indicating how much light is slowed down when passing through the material. A higher refractive index implies stronger light bending, which can lead to sharper and more vibrant images in display technologies. Furthermore, the consistency in the behavior of both the real part (n) and the imaginary part (k) of the complex refractive index across different incident photon energies (as depicted in Figure 7g,h) indicates a uniform response of these compounds to varying light wavelengths. This uniformity is crucial for ensuring consistent optical performance across different wavelengths, thereby enhancing the overall quality and reliability of the display technology.

3.5. Thermodynamic Properties

By investigating the thermodynamic properties such as minimum thermal conductivity, Debye temperature, and melting temperature, we can easily understand how solids respond to heat. The Debye temperature represents a critical point where phonons vibrate at the lowest wavelength, leading to a single mode of vibration. Beyond this temperature, specific heat and internal energy become independent of temperature. To calculate the Debye temperature (θ_D) for UT_2Si_2 (T = Ru, Rh, and Pd), we have employed the well-established equations based on elastic moduli. This equation is as follows:[74]

$$\theta_D = \frac{h}{K_B}\left(\frac{3nN_A\rho}{4\pi M}\right)^{\frac{1}{3}} \times \nu_m \tag{13}$$

The formula for θ_D is based on various parameters such as Planck's constant (h), Boltzmann's constant (K_B), Avogadro's number (N_A), density (ρ), the number of atoms (n), and molar mass (M). The average velocity (ν_m) of sound waves in a crystalline solid can be calculated using:

$$\nu_m = \left[\frac{1}{3}\left(\frac{2}{\nu_s^3} + \frac{1}{\nu_l^3}\right)\right]^{\frac{-1}{3}} \tag{14}$$

where ν_l is the longitudinal and ν_s is the transverse sound velocities, which can be calculated by the Navier's equation:[75]

$$\nu_l = \left(\frac{3B + 4G}{3\rho}\right)^{\frac{1}{2}} \quad \text{and} \quad \nu_s = \left(\frac{G}{\rho}\right)^{\frac{1}{2}} \tag{15}$$

where B and G are bulk and shear modulus, respectively.

The calculated Debye temperature together with sound velocities and density for UT_2Si_2 (where T = Ru, Rh, and Pd) are presented in **Table 6** and depicted in **Figure 8**a. Materials with higher Debye temperatures typically demonstrate superior thermal conductivity, as they offer a broader range of phonon energies available for thermal transport. From the calculated data as shown in Table 6, it is very obvious that the materials URu_2Si_2 and URh_2Si_2 carry comparatively high Debye temperature than UPd_2Si_2 confirming that they are more thermally conductive than UPd_2Si_2. Since the material UPd_2Si_2 exhibits the lowest Debye temperature among the studied compounds therefore it suggests that the thermal conductivity of UPd_2Si_2 is relatively low, indicating its potential suitability as a TBC material.

In this study, we utilize an empirical formula developed by Fine et al.[76] to predict the melting temperature (T_m) of UT_2Si_2 (where T = Ru, Rh, and Pd) that can be written as:

Table 6. The calculated parameters include density ρ (in gm cm^{-3}), transverse ν_t (in m s^{-1}), longitudinal ν_l (in m s^{-1}), and average ν_m (in m s^{-1}) sound velocity, Debye temperature θ_D (in K), the minimum thermal conductivity k_{min} (in Wm^{-1} K^{-1}), and melting temperature T_m (in K) of UT_2Si_2 (T = Ru, Rh, and Pd) along with some similar 122 type of compounds.

Compounds	ρ	ν_t	ν_l	ν_m	θ_D	k_{min}	Tm	References
URu_2Si_2	10.373	3008.69	5533.67	3328.56	394.09	0.727	1705.52	This Study
URh_2Si_2	10.402	3128.82	5668.41	3461.97	409.22	0.754	1752.59	
UPd_2Si_2	10.315	2578.72	5012.10	2933.56	340.241	0.629	1601.99	
YPd_2Si_2	5.709	3761.59	6510.92	4179.16	501.94	0.94	1447.1	Remarks[25]
YNi_2Si_2	6.807	3526.22	6176.29	3918.56	454.44	0.87	1448.03	
YRu_2Si_2	6.936	3597.99	6348.33	4000.78	465.33	0.84	1507.8	
YRh_2Si_2	6.899	3001.67	5677.85	3355.38	387.01	0.69	1352.16	
$LaCu_2Si_2$	6.34	3463.87	5825.63	3835.22	445.32	0.80	1778.44	Remarks[26]
$LaRh_2Si_2$	14.32	2266.00	3980.00	2519.00	358.76	0.79	1902.00	
$LaPd_2Si_2$	7.32	2826.00	5236.00	3155.00	355.47	0.62	1717.21	
$LaAg_2Si_2$	7.04	2993.46	5186.47	3323.40	368.60	0.64	1601.20	
$LaPt_2Si_2$	20.76	1518.00	2221.00	1654.00	234.16	0.51	1732.28	
$LaAu_2Si_2$	10.01	2394.42	4414.92	2671.70	295.37	0.51	1664.02	

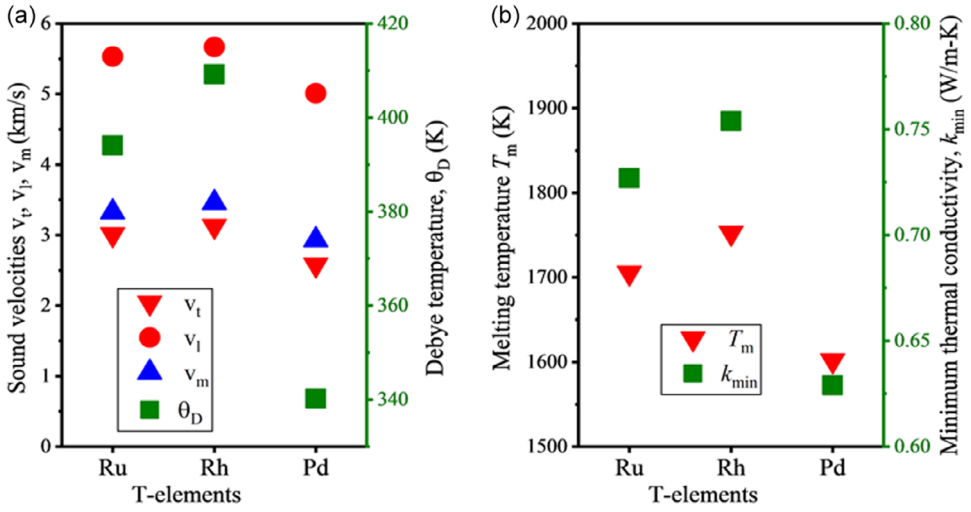

Figure 8. a) The elastic sound velocities and Debye temperature, and b) melting temperature and minimum thermal conductivity variation of UT_2Si_2 (T = Ru, Rh, and Pd).

$$T_m = 354 + \frac{4.5(2C_{11} + C_{33})}{3} \tag{16}$$

The calculated melting temperatures of UT_2Si_2 (T = Ru, Rh, and Pd) are presented in Table 6 and illustrated in Figure 8b. The observed trend reveals an increase in melting temperature as the T-atom progresses from Pd → Ru → Rh, aligning with the descending order of their crystal radii. This variation indicates the influence of atomic size on the stability of URh_2Si_2, which enhances its thermal stability. Furthermore, our findings suggest a strong correlation between melting temperature, Young's modulus, and chemical stability. Materials with higher melting temperatures typically exhibit greater chemical stability, often reflected in higher Young's modulus. Consequently, URh_2Si_2 emerges as a promising candidate for structural materials in extreme conditions, such as high-temperature technology applications.

The minimum thermal conductivity of a material represents its intrinsic ability to conduct heat under ideal conditions, typically at low temperatures. Clark's formula provides a method to determine k_{min}, which is calculated using the equation:[77]

$$k_{min} = k_B \nu_m \left(\frac{M}{n\rho N_A}\right)^{-2/3} \tag{17}$$

In Equation (17), the symbols have the same meanings as in Equation (13). The calculated values of k_{min} are tabulated in Table 6 and depicted in Figure 8b. As we known from thumb

rule that, a material with low Debye temperature has low minimum thermal conductivity.[78] Not only that, materials having low minimum conductivity can be widely used in TBC materials. The calculated values of k_{min} for UT_2Si_2 (T = Ru, Rh, and Pd) are very lower than the widely held TBC material $Y_4Al_2O_9$ (1.13 W mK^{-1}).[79] Furthermore, the K_{min} values of materials UT_2Si_2 (T = Ru, Rh, and Pd) are also smaller than numerous borides like compounds as examples Zr_2AB_2 (A = In, Tl), Hf_2AB_2 (A = In, Sn) and carbide type materials as example Zr_2AC_2 (A = In, Tl) and Hf_2AC (A = In, Sn).[80] So we can say that, the studied materials have more possibility to use in TBC materials than the previously studied boride and carbide type materials. It is remarkable that UPd_2Si_2 exhibits the lowest minimum thermal conductivity among all UT_2Si_2 (T = Ru, Rh, and Pd), making the phase UPd_2Si_2 more suitable for using as TBC applications.

4. Conclusions

In the present study, we have explored the exhaustive physical properties such as structural, bulk, electronic, optical, and thermal features of $ThCr_2Si_2$-type compounds UT_2Si_2 (T = Ru, Rh, and Pd) using the ab initio method found in DFT through the CASTEP discipline. The structural and chemical formations are ensured from enthalpy calculations. The examined elastic stiffness parameters validate the mechanical structural stability condition across all phases. Furthermore, the basic characteristics of polycrystalline materials, including Pugh's ratio and Poisson's ratio, suggest the ductile properties of URu_2Si_2, URh_2Si_2, and UPd_2Si_2. URh_2Si_2 exhibits high Young's modulus, bulk modulus, and hardness, indicating its substantial resistance to volume changes and plastic deformation, making it suitable for industrial use. Conversely, UPd_2Si_2, with its lower Young's modulus, can be used as TBC materials. The high machinability index of UPd_2Si_2 (2.079) among the three indicates its effective use in industry. From the calculations of anisotropic nature, we see that URu_2Si_2 exhibits the greatest anisotropic nature among the studied compounds. Examining the electronic band structures and density of states (PDOS and TDOS) involves analyzing that all compounds are metal with a total density of states ≈6.70, ≈12.78, and ≈8.27 at the Fermi level for URu_2Si_2, URh_2Si_2, and UPd_2Si_2, respectively. Mulliken bond population analysis and charge density maps suggest the existence of both covalent and ionic bonds in all compounds. Various optical characteristics such as dielectric function, refractive index, optical conductivity, reflectivity, absorption, and loss function were examined for UT_2Si_2 (T = Ru, Rh, and Pd) compounds. They perform extraordinary absorption peaks in the UV site approving good absorber in the UV radiation. Hence, they are appropriate for UV optoelectronic devices. The strong reflectivity observed in the UV energy range for these phases confirms their suitability for use as effective solar reflectors within this energy spectrum. The consistent behavior of both real and imaginary parts of the refractive index across different incident photon energies ensures uniform optical performance, enhancing the reliability and quality of display technologies like LCDs and quantum dot TVs. The very low K_{min} values of UT_2Si_2 (T = Ru, Rh, and Pd) compounds than several boride and carbide type materials ensures that these materials can be broadly used in TBC materials.

Acknowledgements

M.A.R. is very grateful to PUST Research Cell for setup the Computational Lab at the Department of Physics in Pabna University of Science and Technology. A.I. extends his appreciation to the Deanship of Research and graduate studies at King Khalid University for funding this work through Large Groups Research Project under grant no. (RGP2/156/45).

Conflict of Interest

The authors declare no conflict of interest.

Author Contributions

Md. Atikur Rahman: conceptualization, supervision, final-editing and validation; **Mst. Asma Khatun**: Formal analysis, drawing figures; **Md. Hasan Mia**: Writing original draft; **Mst. Zugrufa**: Formal Analysis, data formation; **Ahmad Irfan**: Final editing.

Data Availability Statement

The data that support the findings of this study are available on request from the corresponding author. The data are not publicly available due to privacy or ethical restrictions.

Keywords

electronic properties, mechanical properties, optical properties, structural properties, thermodynamic properties

Received: May 9, 2024
Revised: August 11, 2024
Published online:

[1] I. Z. Awan, A. Qadeer Khan, *J. Chem. Soc. Pak.* **2015**, *37*, 1056.
[2] J. Emsley, *Nature's Building Blocks*, Oxford University Press, New York **2001**, pp. 141–142.
[3] Z. Ban, M. Sikirica, *Acta Crystallogr.* **1965**, *18*, 594.
[4] E. Mörsen, B. D. Mosel, W. Müller-Warmuth, M. Reehuis, W. Jeitschko, *J. Phys. Chem. Solids* **1988**, *49*, 785.
[5] D.-B. Kang, *Bull. Korean Chem. Soc.* **2003**, *24*, 1215.
[6] G. Venturini, B. Malaman, B. Roques, *J. Solid State Chem.* **1989**, *79*, 136.
[7] J. González, R. Kessens, H.-U. Schuster, *Z. Anorg. Allgem. Chem.* **1993**, *619*, 13.
[8] M. Rotter, M. Tegel, D. Johrendt, *Phys. Rev. Lett.* **2008**, *101*, 107006.
[9] K. Sasmal, B. Lv, B. Lorenz, A. M. Guloy, F. Chen, Y.-Y. Xue, C.-W. Chu, *Phys. Rev. Lett.* **2008**, *101*, 107007.
[10] B. Lv, L. Deng, M. Gooch, F. Wei, Y. Sun, J. K. Meen, Y.-Y. Xue, B. Lorenz, C.-W. Chu, *Proc. Natl. Acad. Sci.* **2011**, *108*, 15705.
[11] T. T. M. Palstra, G. Lu, A. A. Menovsky, G. J. Nieuwenhuys, P. H. Kes, J. A. Mydosh, *Phys. Rev. B* **1986**, *34*, 4566.
[12] E. Karaca, H. M. Tütüncü, G. P. Srivastava, S. Uğur, *Phys. Rev. B* **2016**, *94*, 054507.
[13] R. N. Shelton, H. F. Braun, E. Musick, *Solid State Commun.* **1984**, *52*, 797.

[14] M. Vališka, J. Pospíšil, J. Prokleška, M. Diviš, A. Rudajevová, V. Sechovský, *J. Phys. Soc. Jpn* **2012**, *81*, 104715.
[15] H. Fujii, A. Sato, *J. Alloys Compd.* **2009**, *487*, 198.
[16] V. K. Anand, H. Kim, M. A. Tanatar, R. Prozorov, D. C. Johnston, *J. Phys.: Condens. Matter* **2014**, *26*, 405702.
[17] V. K. Anand, H. Kim, M. A. Tanatar, R. Prozorov, D. C. Johnston, *Phys. Rev. B* **2013**, *87*, 224510.
[18] H. Fujii, A. Sato, *Phys. Rev. B* **2009**, *79*, 224522.
[19] M. B. Maple, J. W. Chen, Y. Dalichaouch, T. Kohara, C. Rossel, M. S. Torikachvili, M. W. McElfresh, J. D. Thompson, *Phys. Rev. Lett.* **1986**, *56*, 185.
[20] R. Marazza, R. Ferro, G. Rambaldi, G. Zanicchi, *J. Less. Common. Met.* **1977**, *53*, 193.
[21] F. Parvin, S. H. Naqib, *J. Alloys Compd.* **2019**, *780*, 452.
[22] X. Gui, T.-R. Chang, T. Kong, M. T. Pan, R. J. Cava, W. Xie, *Materials* **2017**, *10*, 818.
[23] M. U. Salma, M. A. Rahman, *Int. J. Mod. Phys. B* **2018**, *32*, 1850357.
[24] K. Ciesielski, G. Chajewski, M. Samsel–Czekała, A. Hackemer, P. Obstarczyk, A. P. Pikul, D. Kaczorowski, *Solid State Commun.* **2018**, *280*, 13.
[25] M. A. Rahman, M. Hasan, J. F. Lubna, R. Khatun, S. Sarker, M. Z. Hasan, A. Hossain, Md. M. Hossain, Md. Rasheduzzaman, W. Hasan, N. Jamila, *J. Phys. Chem. Solids* **2023**, *178*, 111342.
[26] M. A. Rahman, R. Khatun, R. Ferdous, D. C. Roy, M. Z. Hasan, A. Irfan, M. A. R. Sarker, Md. M. Hossain, A. Hossain, S. C. Mouna, S. Sarker, *J. Mater. Res. Technol.* **2023**, *26*, 3840.
[27] S. J. Clark, M. D. Segall, C. J. Pickard, P. J. Hasnip, M. I. J. Probert, K. Refson, M. C. Payne, *Z. Krist.-Cryst. Mater.* **2005**, *220*, 567.
[28] M. D. Segall, P. J. D. Lindan, M. J. al Probert, C. J. Pickard, P. J. Hasnip, S. J. Clark, M. C. Payne, *J. Phys.: Condens. Matter* **2002**, *14*, 2717.
[29] J. P. Perdew, K. Burke, M. Ernzerhof, *Phys. Rev. Lett.* **1996**, *77*, 3865.
[30] D. Vanderbilt, *Phys. Rev. B* **1990**, *41*, 7892.
[31] H. J. Monkhorst, J. D. Pack, *Phys. Rev. B* **1976**, *13*, 5188.
[32] T. H. Fischer, J. Almlof, *J. Phys. Chem.* **1992**, *96*, 9768.
[33] M. A. Hadi, S.-R. G. Christopoulos, A. Chroneos, S. H. Naqib, A. K. M. A. Islam, *Sci. Rep.* **2022**, *12*, 14037.
[34] R. Gaillac, P. Pullumbi, F.-X. Coudert, *J. Phys.: Condens. Matter* **2016**, *28*, 275201.
[35] B. Saparov, A. S. Sefat, *J. Solid State Chem.* **2013**, *204*, 32.
[36] Z. T. Y. Liu, D. Gall, S. V. Khare, *Phys. Rev. B* **2014**, *90*, 134102.
[37] Z. T. Y. Liu, X. Zhou, S. V. Khare, D. Gall, *J. Phys.: Condens. Matter* **2013**, *26*, 025404.
[38] Z. T. Y. Liu, X. Zhou, D. Gall, S. V. Khare, *Comput. Mater. Sci.* **2014**, *84*, 365.
[39] F. Birch, *Phys. Rev.* **1947**, *71*, 809.
[40] F. D. Murnaghan, *Proc. Natl. Acad. Sci.* **1944**, *30*, 244.
[41] I. R. Shein, A. L. Ivanovskii, *Solid State Commun.* **2011**, *151*, 1165.
[42] M. Born, K. Huang, *Dynamical Theory of Crystal Lattices*, Oxford University Press, Oxford **1996**.
[43] M. A. Hadi, S.-R. G. Christopoulos, A. Chroneos, S. H. Naqib, A. K. M. A. Islam, *Sci. Rep.* **2022**, *12*, 1.
[44] W. Voigt, *Lehrbuch der Kristallphysik (Textbook of Crystal Physics)*, BG Teubner, Leipzig und Berlin **1928**.
[45] A. Reuss, Z. Angnew, *Math. Meth.* **1929**, *9*, 55.
[46] R. Hill, *Proc. Phys. Soc.* **1952**, *65*, 350.
[47] R. Hill *Proc. Phys. Soc. A* **1952**, *65*, 349.
[48] X.-Q. Chen, H. Niu, D. Li, Y. Li, *Intermetallics* **2011**, *19*, 1275.
[49] X. Wang, H. Xiang, X. Sun, J. Liu, F. Hou, Y. Zhou, *J. Mater. Sci. Technol.* **2015**, *31*, 369.
[50] S. F. Pugh, *London Edinburgh Dublin Philos. Mag. J. Sci.* **1954**, *45*, 823.
[51] I. N. Frantsevich, *Elastic Constants and Elastic Moduli of Metals and Insulators*, Reference Book **1982**.
[52] M. I. Naher, S. H. Naqib, *Sci. Rep.* **2021**, *11*, 5592.
[53] Z. Sun, D. Music, R. Ahuja, J. M. Schneider, *Phys. Rev. B* **2005**, *71*, 193402.
[54] R. C. Lincoln, K. M. Koliwad, P. B. Ghate, *Phys. Rev.* **1967**, *157*, 463.
[55] L. Vitos, P. A. Korzhavyi, B. Johansson, *Nat. Mater.* **2003**, *2*, 25.
[56] M. J. Phasha, P. E. Ngoepe, H. R. Chauke, D. G. Pettifor, D. Nguyen-Mann, *Intermetallics* **2010**, *18*, 2083.
[57] H. Ledbetter, A. Migliori, *J. Appl. Phys.* **2006**, *100*, 063516.
[58] M. W. Barsoum, M. Radovic, *Annu. Rev. Mater. Res.* **2011**, *41*, 195.
[59] M. I. Naher, F. Parvin, A. K. M. A. Islam, S. H. Naqib, *Eur. Phys. J. B* **2018**, *91*, 289.
[60] M. D. Segall, R. Shah, C. J. Pickard, M. C. Payne, *Phys. Rev. B* **1996**, *54*, 16317.
[61] D. Sanchez-Portal, E. Artacho, J. M. Soler, *Solid State Commun.* **1995**, *95*, 685.
[62] R. S. Mulliken, *J. Chem. Phys.* **1955**, *23*, 1833.
[63] R. P. Singh, *J. Magnes. Alloys* **2014**, *2*, 349.
[64] M. A. Ali, M. A. Hadi, M. M. Hossain, S. H. Naqib, A. K. M. A. Islam, *Phys. Status Solidi B* **2017**, *254*, 1700010.
[65] M. A. Green, Y. Jiang, A. M. Soufiani, A. Ho-Baillie, *J. Phys. Chem. Lett.* **2015**, *6*, 4774.
[66] C. Ambrosch-Draxl, J. O. Sofo, *Comput. Phys. Commun.* **2006**, *175*, 1.
[67] N. V. Smith, *Phys. Rev. B* **1971**, *3*, 1862.
[68] N. Hasan, M. Arifuzzaman, A. Kabir, *RSC Adv.* **2022**, *12*, 7961.
[69] L. H. Ame, M. A. Rahman, *J. Control Instrum. Eng.* **2020**, *6*.
[70] A. Alabastri, S. Tuccio, A. Giugni, A. Toma, C. Liberale, G. Das, F. De Angelis, E. Di Fabrizio, R. P. Zaccaria, *Materials* **2013**, *6*, 4879.
[71] M. M. Obeid, M. M. Shukur, S. J. Edrees, R. Khenata, M. A. Ghebouli, S. A. Khandy, A. Bouhemadou, H. R. Jappor, X. Wang, *Chem. Phys.* **2019**, *526*, 110414.
[72] R. Khatun, M. A. Rahman, K. M. Hossain, M. Z. Hasan, M. Rasheduzzaman, S. Sarker, *Phys. B* **2021**, *620*, 413258.
[73] J. K. Rony, M. Islam, M. Saiduzzaman, K. M. Hossain, S. Alam, A. Biswas, M. H. Mia, S. Ahmad, S. K. Mitro, *J. Mater. Res. Technol.* **2024**, *29*, 897.
[74] D. H. Chung, W. R. Buessem, *J. Appl. Phys.* **2010**, *38*, 1967.
[75] C. Li, Z. Wang, *Advances in Science and Technology of Mn+1AXn Phases*, Woodhead Publishing, Cambridge **2012**, pp. 197–222.
[76] M. E. Fine, L. D. Brown, H. L. Marcus, *Scr. Metall.* **1984**, *18*, 951.
[77] D. R. Clarke, *Surf. Coat. Technol.* **2003**, *163*, 67.
[78] A. N. Rima, M. A. Rahman, R. Ferdous, M. N. M. Nobin, M. Ferdous Rahman, *Comput. Condens. Matter.* **2024**, *39*, e00900.
[79] Y. Zhou, X. Lu, H. Xiang, Z. Feng, *J. Adv. Ceram.* **2015**, *4*, 94.
[80] M. A. Ali, M. M. Hossain, M. M. Uddin, A. K. M. A. Islam, S. H. Naqib, *J. Mater. Res. Technol.* **2021**, *15*, 2227.